International Journal of Greenhouse Gas Control 74 (2018) 49–61

Contents lists available at ScienceDirect

International Journal of Greenhouse Gas Control

journal homepage: www.elsevier.com/locate/ijggc

Swelling stress development in confined smectite clays through exposure to CO_2

M. Zhang[a,*], S.M. de Jong[a], C.J. Spiers[a], A. Busch[b], H.M. Wentinck[c]

[a] HPT Laboratory, Faculty of Geosciences, Utrecht University, Budapestlaan 4, 3584 CD Utrecht, The Netherlands
[b] The Lyell Centre for Earth and Marine Science and Technology, Heriot-Watt University, Edinburgh EH14 4AS, Scotland, United Kingdom
[c] Shell Global Solutions International B.V., Kesslerpark 1, 2288 GS Rijswijk, The Netherlands

ARTICLE INFO

Keywords:
CO_2 storage
Caprock integrity
Clay swelling
Swelling stress

ABSTRACT

Recent work has shown that unconfined smectite clays swell upon exposure to supercritical (SC) CO_2 due to uptake in the clay interlayer region. Such swelling behaviour is expected to cause internal stress development under geometrically confined conditions pertaining to geological storage of CO_2, but this has not been widely investigated. Here, we report uniaxial compaction/swelling tests performed, using a 1-D compaction cell, on pre-pressed discs of Wyoming (Na-SWy-1) and Arizona (Ca-SAz-1) montmorillonite, as well as on smectite-bearing shale. We explore the axial (Terzaghi) effective stress generated in these materials upon exposure to 10 MPa CO_2 pressure under conditions where total swelling (including poroelastic effects) is restricted to axial strains below 3%. The experiments were performed at 44 °C. In each experiment, the sample was first equilibrated with lab air (RH ≈ 40%–60% at T = 20–25 °C) at the experimental temperature and pre-compacted at ~60 MPa axial stress to generate a dense reproducible microstructure. A lower axial normal stress of 25.9–40.9 MPa was then applied and the loading piston held in fixed position. This yielded an effective (Terzaghi) overburden stress of 9.6–24.7 MPa upon introduction of CO_2 at 10 MPa, thus simulating burial depths of ~0.8–2.0 km. Following CO_2 introduction, axial swelling stresses developed rapidly, independently of the direct effect of increased pore pressure, attaining values of 7.1–12.4 MPa at equilibrium, compared with ~2 MPa obtained using inert Ar. Experiments on Na-SWy-1 montmorillonite showed that the swelling stress generated upon exposure to CO_2 decreases with increasing initial and final effective normal stress, suggesting that overburden stress suppresses swelling (stress) development in smectite, presumably by limiting the amount of CO_2 uptake by the material investigated. The swelling stresses observed imply that CO_2 penetration into caprocks and faults in geological storage systems will lead to an increase in effective normal stress components, which in turn will tend to promote closure of fractures and enhance sealing integrity. However, further work is needed to improve understanding of the processes underlying the swelling of smectite caused by CO_2 and to evaluate any risks posed to caprock and fault integrity by swelling-induced shear stresses.

1. Introduction

Long-term storage of carbon dioxide in deep geological formations presents an important option for reducing emissions of anthropogenic greenhouse gases into the atmosphere (Hepple and Benson, 2005; Holloway, 1997), that is gaining new momentum since the 2016 Paris Climate Agreement (UNFCCC, 2016). One of the main knowledge gaps in this field relates to the processes occurring when supercritical CO_2 migrates slowly into the low permeability fracture and pore networks present in caprocks and faults. In particular, little is known regarding the long-term effects of CO_2 storage on caprock and fault sealing integrity (Gaus, 2010; Shukla et al., 2010). Many potential storage reservoirs are sealed by mudrock or shale caprocks, the generally low permeability of which is predominantly caused by the presence of clay minerals (Song and Zhang, 2013). Smectites (i.e. swelling clays, such as montmorillonites) are common constituents of such rocks and are often present in faults that laterally seal potential storage reservoirs, at least at depths up to about 2–3 km (80 °C). At greater depths, smectites generally start to transform to the non-swelling clay mineral, illite (Colten-Bradley, 1987; Lynch, 1997; Hover et al., 1976). Large sedimentary basins, such as in the North Sea, frequently contain large amounts of smectite that sometimes even dominate the total clay mineralogy as well as the mineralogy of individual argillite units (Horsrud et al., 1998; Pearson, 1990). The North Sea is considered to be the main

* Corresponding author.
E-mail address: m.zhang@uu.nl (M. Zhang).

https://doi.org/10.1016/j.ijggc.2018.04.014
Received 29 August 2017; Received in revised form 7 April 2018; Accepted 14 April 2018
Available online 30 April 2018
1750-5836/

Table 1
List of the complete set of swelling stress experiments and key data obtained in this study.

Series-Exp No.	Material	Pore fluid	Sample humidity	Pre-compaction *stress* σ_{pre} *MPa*	Starting normal stress σ_{start} *MPa*	σ_e^{in} *MPa*	Equivalent burial depth *km*	$\Delta\sigma^e$ *MPa*	σ_{sw} *MPa*	σ_e^{eq} *MPa*	x_{sw} *mm*
S1-M1	Na-SWy-1	CO_2	Lab air dry	60.37	27.24	10.97	0.88	16.27	10.03	21.00	NR
S1-M2	Na-SWy-1	CO_2	Lab air dry	60.37	34.20	18.95	1.52	15.25	8.60	27.58	NR
S1-M3	Na-SWy-1	CO_2	Lab air dry	60.37	39.67	22.84	1.83	16.83	8.00	30.84	NR
S1-M4	Ca-SAz-1	CO_2	Lab air dry	60.37	34.60	18.49	1.48	16.11	12.41	30.90	NR
S1-M5	Smectite shale	CO_2	Lab air dry	60.37	40.85	24.71	1.98	16.14	9.30	34.01	NR
S2-M6	Na-SWy-1	CO_2	Lab air dry	60.37	25.90	9.63	0.77	16.27	10.77	20.40	0.0194
S2-M7	Na-SWy-1	CO_2	Lab air dry	60.37	28.90	12.76	1.02	16.14	9.45	22.28	0.0180
S2-M8	Na-SWy-1	CO_2	Lab air dry	60.37	31.61	14.41	1.15	17.20	9.08	24.50	0.0170
S2-M9	Na-SWy-1	CO_2	Lab air dry	60.37	35.30	18.1	1.45	17.20	8.30	26.40	0.0153
S2-M10	Na-SWy-1	CO_2	Lab air dry	60.37	35.20	18.96	1.52	16.24	8.60	27.56	0.0160
S2-M11	Na-SWy-1	CO_2	Lab air dry	60.37	35.60	19.23	1.54	16.37	8.03	27.27	0.0144
S2-M12	Na-SWy-1	CO_2	Lab air dry	60.37	38.90	22.56	1.80	16.34	7.05	29.60	0.0137
S2-M13	Na-SWy-1	CO_2	Lab air dry	60.37	39.13	22.93	1.83	16.20	7.43	30.36	0.0130
S3-M1	Na-SWy-1	Ar	Lab air dry	60.37	28.64	11.92	0.95	16.72	2.51	14.43	0.0069
S3-M2	Na-SWy-1	Ar	Lab air dry	60.37	29.97	12.34	0.99	16.63	3.13	15.47	0.0082
S3-M3	Na-SWy-1	Ar	Lab air dry	60.37	34.53	18.04	1.51	16.49	2.99	21.03	0.0071

All experiments listed in the table were performed at a nominal temperature of 44(± 1.5) °C, and pore fluid pressure of 10(± 0.2) MPa. Note that σ_{pre} indicates the stress applied to the sample in the pre-compaction stage, while σ_{start} is the subsequently imposed normal stress on the sample before CO_2 injection. This normal stress σ_{start} was pre-determined to obtain realistic effective overburden stresses (σ_e^{in}) upon injection of CO_2 at 10 MPa pressure, taking into account machine deformation upon injection. σ_e^{in} is the initial effective normal stress, resulting from the introduction of CO_2 at a pressure of 10 MPa for each sample tested, as calculated from our machine calibration data independently of any swelling stress development. $\Delta\sigma^e$ is the difference between σ_{start} and σ_e^{in}, i.e. change in effective stress supported by the sample upon CO_2 pressurization. The equivalent (simulated) burial depth for each sample was calculated assuming sedimentary rock with an average density of 2250 kg/m^{-3} and the presence of a hydrostatic pore fluid pressure gradient. σ_{sw}, σ_e^{eq}, x_{sw} are respectively the (apparent) equilibrium swelling stress developed, the effective normal stress supported by the sample at (apparent) equilibrium, and the corresponding swelling deformation, which are calculated from the average value of load and LVDT signals collected in the 0.5–2 h before the termination of each experiment.
S1 and S2 series of experiments are performed with CO_2 as pore fluid, while S3 series are conducted using Ar, to calibrate the swelling effect associated with poro-elastic effects.
NR represents "not reported" due to unacceptably large errors associated with the external LVDT used in the S1 experiments (only).

target for offshore storage of CO_2 in Europe. This makes the interaction between CO_2 and swelling clays an important and timely topic to investigate (Busch et al., 2016; Espinoza and Santamarina, 2012).

The crystal structure of smectites is characterized by alternating tetrahedral and octahedral silicate sheets separated by an interlayer "gallery" region. Solid solution substitutions in the silicate sheet structure impart excess negative charge, which attracts charge-balancing cations and an associated cage of water molecules into the interlayer region (Sato et al., 1992). Uptake of these water molecules, in layers up to three molecules thick, causes the structure to expand or shrink normal to the silicate sheets, depending on temperature, pressure, water activity and clay composition (Xu et al. 2000; Sato et al., 1992; Sposito and Prost, 1982; Prost et al. 1998; Harward and Brindley, 1965; Bishop et al., 1994). This expansion is referred to as clay swelling and is known to occur in a stepwise manner (Mooney et al., 1952; Norrish, 1954), giving rise to specific values of the interlayer spacing or d_{001}–spacing, corresponding to uptake of 1, 2 or 3 discrete layers of water molecules.

Recent experimental studies (Giesting et al., 2012a,b; Schaef et al., 2012, 2015; Ilton et al., 2012; Loring et al., 2012, 2014; Rother et al., 2013; De Jong et al., 2014; Michels et al., 2015;) have shown that besides the well-known swelling effects, seen when smectites take up interlayer water, smectites can also swell by a few percent when exposed to supercritical CO_2 under unconfined hydrostatic conditions. This swelling is attributed to interlayer uptake of CO_2 via adsorption, which can be significant depending on the clay mineral type and its hydration state (Busch et al., 2016). The effect occurs if the initial hydration state of the smectites is intermediate between 'n' and "n + 1′ complete hydration layers. For example, SWy-1 montmorillonite swells when charged with CO_2 at initial hydration states between fully dry (basal d-spacing $d_{001} \leq 10.0$ Å) and having one water layer in the smectite interlayer structure ($d_{001} \approx 12.4$ Å) (c.f. Giesting et al., 2012a; De Jong et al., 2014). Ca-montmorillonites show similar behaviour at hydration states between 0 and 1 and between 1 and 2 water layers (c.f. Giesting et al., 2012b; Schaef et al., 2012). These intermediate hydration states are believed to exist at the pressure-temperature conditions typical of potential CO_2 storage sites located at depths up to 2–3 km (e.g. Bird 1984), especially in caprocks that are not fully water saturated, such as those overlying depleted oil and gas reservoir system.

However, whereas CO_2-induced swelling has been observed in experiments conducted under mechanically unconfined conditions (sample surrounded by hydrostatic CO_2 pressure and free to swell), no data exist on the relationship between stress state and CO_2-induced swelling of smectite minerals under confined conditions, i.e. where the material is subjected to an existing effective stress and is not free to swell. Under in-situ conditions, rock is unable to swell freely, especially laterally. This means that an increase in effective stress components, i.e. a self-stressing effect, can be expected which could potentially close CO_2-filled pores and cracks in caprocks and faults, thus enhancing their sealing capacity, or else cause mechanical damage which would reduce seal integrity if deviatoric stresses become large enough. On the other hand, the stress experienced by the solid framework might suppress CO_2 uptake, as recently reported for CO_2 sorption in coal (e.g. Hol et al., 2011, 2012; Liu et al., 2016).

In the present study, we investigated the stresses that develop when smectites are exposed to supercritical CO_2 under conditions where swelling is restricted and under pressure, temperature and smectite hydration conditions similar to those expected in subsurface CO_2 storage systems. We approached this by means of laterally confined, uniaxial compression (1-D strain) experiments performed on samples of well-characterized montmorillonite, a common upper crustal smectite, plus one further test on smectite-bearing shale. The tests were conducted by introducing supercritical CO_2 into pre-pressed discs of these materials at ~44 °C and at axial stresses simulating burial depths of ~0.8 to 2.0 km. Here, we report changes in the (Terzaghi) effective stress that occurred due to sample swelling in the axial direction (including poro-elastic effects), which we term the swelling stress. We go on to consider the implications for CO_2 storage.

2. Experimental approach

Three series of laterally confined compression/swelling experiments were performed (see Table 1), using a 1-D compaction vessel to allow axial loading with zero lateral strain. The first series of experiments (Series S1), performed on sample numbers 1–5 (denoted S1-M1 to S1-M5), was primarily aimed at investigating the development of swelling stress in different smectite (bearing) materials (Na-SWy-1 montmorillonite, Ca-SAz-1 montmorillonite and smectite shale) under a fixed initial vertical (i.e. axial) stress. The second series (S2), performed on sample numbers 6–13 (denoted S2-M6 to S2-M13), focused on Na-SWy-1 montmorillonite samples subjected to different initial axial stresses (simulated overburden stress). This series was aimed at providing additional data on the effect of overburden stress on swelling stress development, with increased accuracy in measuring small associated swelling strains. In addition, 3 swelling stress tests (Series 3, S3-M1 to S3-M3) were performed on Na-SWy-1 samples using Ar at 10 MPa, assuming this to behave as an inert pore-fluid that does not penetrate into clay interlayer structure (Eltantawy and Arnold, 1972). These control experiments were performed to quantify poro-elastic stress changes due to pore fluid pressurization, independently of CO_2-related swelling. In each of these control tests, cyclic loading and unloading was conducted after swelling stress measurement, to provide representative data on the uniaxial stiffness modulus of the present samples.

2.1. Starting materials and gases

As indicated above, the experiments were conducted on two types of naturally occurring montmorillonites, namely Na-rich Wyoming type (Na-SWy-1) and Ca-rich Arizona type (Ca-SAz-1). These were obtained from the Source Clays Repository of The Clay Minerals Society and have been extensively characterized in the past (e.g. Van Olphen and Fripiat, 1979). Na-SWy-1 is a low charge montmorillonite with solid substitutions occurring in both the tetra- and octahedral sheet; the interlayer cation largely consists of sodium. Ca-SAz-1 is a high charge montmorillonite with solid substitutions occurring solely in the tetrahedral sheet. The interlayer cations present in this montmorillonite are mainly calcium, with smaller amounts of potassium and sodium. Note that no attempt was made to purify the samples by cation exchange procedures. The two montmorillonites were used, in 'as received' powder form, without any chemical pre-treatment or grain size fractionation. One additional experiment was conducted on a typical smectite-bearing shale, from a North Sea gas field, for which XRD analysis showed the smectite content to be 53%. The remaining constituents of the shale were illite (13.7%), kaolinite (11.5%), quartz (11.7%) and smaller quantities of calcite, plagioclase and chlorite (less than 7% in total). This material was crushed prior to use, using a pestle and mortar, until finer than the mesh of a 37 μm sieve.

All swelling stress experiments were conducted using 99.999% pure CO_2. The control experiments were performed with 99.99% pure Ar. Both fluids were supplied by Air Products NL.

2.2. Sample preparation

The experiments were performed on disc-shaped samples of the clay-bearing materials investigated. The samples were pre-formed and subsequently pre-compacted and then tested in the titanium sample vessel shown in Fig. 1a. Pre-forming was accomplished as follows. First, ~0.15 g of sample powder was distributed evenly in the titanium vessel (inner diameter ϕ_{inn} = 12.15 mm, outer diameter ϕ_{out} = 19.1 mm; Liteanu and Spiers, 2009). This was then lightly compressed by hand between the upper and lower titanium pistons to yield a flat, disc-shaped sample of ~1 mm thickness. A 1 mm thick circular Titanium porous plate (diameter = 12.15 mm, porosity ~50%, pore size ~5 μm), was subsequently placed between the sample and upper Titanium piston, to act as a filter and fluid distributor. The titanium vessel, plus sample, Ti porous plate and pistons (referred to henceforth as the sample assembly), were then transferred to the main experimental apparatus.

2.3. Experimental apparatus

Swelling stress was measured by exposing the disc-shaped samples to a CO_2 pressure of ~10 MPa under mechanical conditions that prevented the samples from swelling laterally and vertically (other than for small amounts of machine distortion). To achieve this, an oedometer-type pressure vessel (i.e. a 1-D compaction vessel) made of hardened stainless steel (Remanit 4122) was used to house the Ti vessel and sample assembly (Fig. 1a), applying axial load and/or imposing fixed position boundary conditions to the sample assembly, using an Instron 8862 servo-controlled testing machine (Fig. 1b).

In this set-up, the titanium sample assembly (Fig. 1a) was axially loaded via two Remanit pistons (diameter 19.1 mm) sealed against the Remanit vessel with Viton O-rings. The temperature of the system was controlled using an external furnace. This was regulated by means of a Eurotherm temperature controller connected to a type K thermocouple located in the external furnace windings. Sample temperature was measured using a second type K thermocouple placed in a small recess in the outer Remanit pressure vessel at a distance of ~0.5 mm from the titanium sample vessel. Axial load was measured externally, using a 100 kN Instron load cell mounted on the Instron cross-head above the upper Remanit pistons (Fig. 1b). Piston displacement (sample thickness change) plus overall machine deformation was measured using a displacement transducer (linear variable differential transformer-LVDT) located in the Instron loading ram (internal LVDT). Displacement of the upper Remanit piston relative to the top surface of the compaction vessel, hence the deformation occurring in the sample plus all components located between the top Remanit piston and the bottom Remanit piston, was measured using a second external LVDT (Fig. 1b). In the first series of experiments (S1-M1 to S1-M5), an external LVDT with a full scale displacement of 2 mm and a resolution of ± 0.25 μm was used. In the second series (S2-M6 to S2-M13) and third series (S3-M1 to S3-M3), this was replaced by a more sensitive type (Solartron, Model-DFg1) with a full scale displacement of 2 mm and effective resolution < 0.1 μm.

In the Series 1 and Series 2 experiments, CO_2 pressure was applied to the samples through a CO_2 inlet in the upper Remanit piston, as shown in Fig. 1b. CO_2 was initially supplied from a CO_2 cylinder (5 MPa) via a line regulator and valve, and then further pressurized to and controlled at 10 MPa using a separator. This was primed with CO_2 on the sample side and backed with Argon supplied from a regulated (20 MPa) cylinder. For accurate pressure measurement near the sample, a Honeywell MSI (0–35 MPa) pressure transducer was placed adjacent to the CO_2 inlet pipe at the entry-point to the upper Remanit piston.

The Series 3 control experiments, performed with Ar, used the same set-up as that employed in the second series of swelling stress experiments. In this case, however, the Ar pore fluid was directly introduced from a gas cylinder (bottle pressure ~20 MPa) via the CO_2 inlet as shown in Fig. 1b, with the pressure being adjusted and maintained by a regulator installed to the outlet of the gas bottle.

In all three series of experiments, the internal and external LVDT signal, axial load, temperature and CO_2 pressure signals were logged digitally, at a frequency of 1 Hz, using a National Instruments VI Logger system plus PC.

2.4. Testing procedure

2.4.1. Series 1 and 2 experiments

Following sample preparation, the titanium sample assembly was placed in the pressure vessel and the top piston was emplaced. The entire compaction set-up was then mounted into the Instron loading frame. The assembly was subsequently heated to 44 ± 1.5 °C, with the

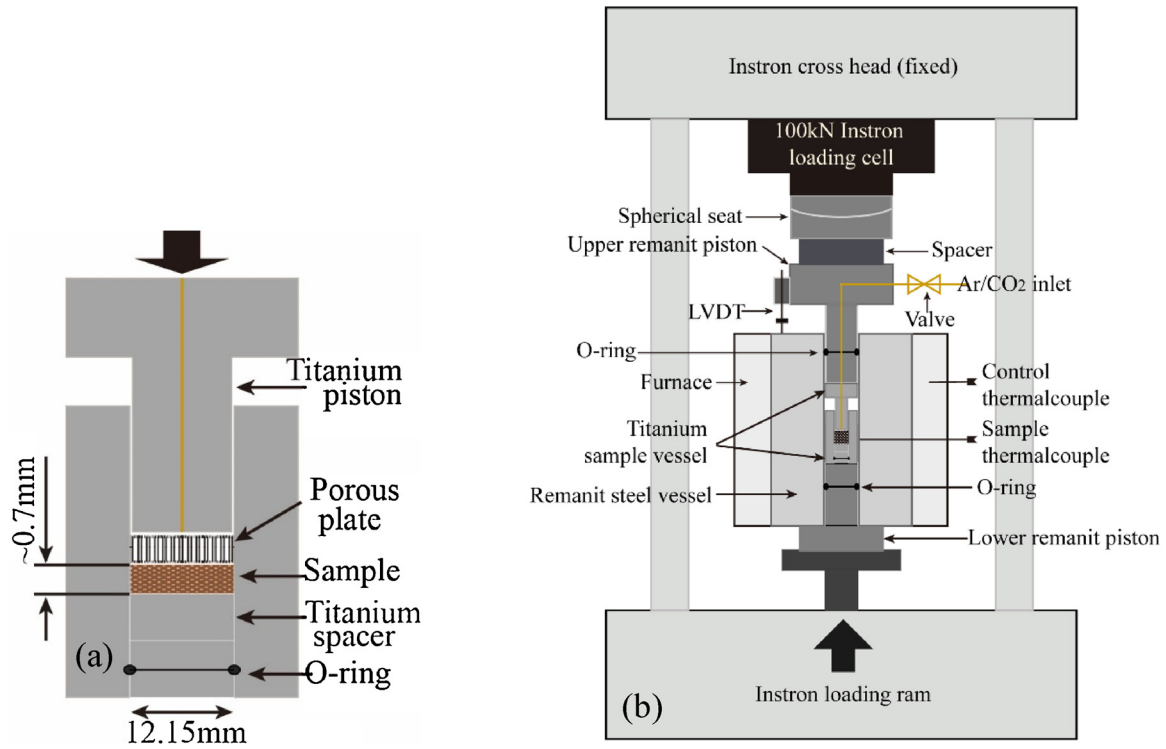

Fig. 1. Schematic representation of the set-up used for measuring the swelling stress generated in pre-pressed smectite discs upon exposure to supercritical-CO_2. (a) Sample assembly including sample housed in Ti die/vessel, upper Ti piston with central bore, a Ti porous plate (1 mm thick) allowing pore fluid access to the sample and a Ti lower piston/spacer; (b) Uniaxial loading system. Sample assembly is located and loaded within in the Remanit stainless steel compaction vessel. In the first and second series of experiments, CO_2 pressure was injected into the sample through the upper piston column (and Ti porous plate). CO_2 pressure was controlled using a separator primed with CO_2 connected to the CO_2 inlet, with the other side backed up by Ar regulated at 10 MPa pressure. In the third series of (control) experiments, Ar gas was directly injected from an Ar cylinder into the sample.

sample and pore fluid system drained to lab air to allow equilibration with the ambient relative humidity RH = 40-60%, using the Instron to apply a small load to the sample. This temperature was chosen to ensure that the initial hydration state of the smectite, at ambient RH, would fall at a level between zero and one interlayer of water molecules for Na-SWy-1, and one to two layers of interlayer water molecules for Ca-SAz-1, noting that the specific d_{100}–spacing achieved is difficult to constrain (De Jong et al., 2014; Ferrage et al., 2007). When thermally equilibrated, a pre-compaction load was applied to create samples of fixed initial thickness (~0.6–0.7 mm). In each of the individual Series 1 and Series 2 experiments performed (on Na-SWy-1, Ca-SAz-1 and smectite shale), a pre-compaction stress (σ_{pre}) of ~60 MPa was applied for about four hours, during which time the sample first compacted rapidly, with the compaction rate decreasing with time until little or no creep was observed. Pre-compaction was done to ensure that all samples tested experienced the same initial loading history and to eliminate permanent compaction effects due to frictional/ductile flow at lower applied stresses. Given the mass of the samples and their dimensions after pre-compaction, in comparison with the dry grain density of the Na-SWy-1 and Ca-SAz-1 clays (~2.2 g/cm^3), the bulk porosity of the pre-compacted samples was around 15–25%. After pre-compaction, the applied axial stress was reduced to a starting value (σ_{start}) varying in the range of 26–41 MPa (Table 1), to achieve simulated overburden stresses expected at depths of about 1–2 km. The Instron machine was then set in position control mode at a fixed ram position, hence restricting the sample from swelling. The CO_2 inlet was subsequently attached to the pore fluid system and CO_2 was introduced into the sample and CO_2 separator from the CO_2 cylinder. The CO_2 pressure was then gradually increased from 0 to 5 MPa (bottle pressure), using the CO_2 cylinder regulator. Further increase in the pore fluid pressure (CO_2) was achieved incrementally, via the Ar backing system, over several minutes, to the final target of 10 MPa, at which it was subsequently held constant within ± 0.2 MPa.

Throughout this paper, we use Terzaghi's definition for the effective stress (σ_e) supported by the sample, i.e. $\sigma_e = (\sigma_n - P)$, where σ_n is the normal stress applied by the piston to the sample, and P is the pore fluid pressure present in the sample. Upon the introduction of CO_2, the effective axial stress supported by the sample decreased instantly, due to the combined effects of CO_2 pressurization and machine deformation, by an amount that could be calculated to an accuracy of within ~0.4 MPa from the calibrations described below. The resulting effective axial stress, calculated at the instant of CO_2 introduction at 10 MPa, will be referred to henceforth as the initial effective stress (σ_e^{in}, see Table 1). Following CO_2 introduction, axial force was monitored to determine the evolution of effective stress supported by the sample. The value measured in excess of the initial effective stress (σ_e^{in}) is defined as the swelling stress in the present study, and includes the effects of both CO_2 uptake-induced swelling and poro-elastic expansion of the sample. When the monitored signal remained stable over time, the experiments were terminated by depressurization of the CO_2, followed by unloading the samples axially, cooling and disassembly.

Note that in all experiments, the applied initial effective stress as well as the maximum value attained during testing were always lower than the 60 MPa stress applied during pre-compaction, thus minimizing any additional mechanical compaction of the sample during the main testing phase.

2.4.2. Series 3 experiments

In the Series 3 control experiments, the Na-SWy-1 samples tested were prepared and pre-compacted using the same method and under identical temperature and RH conditions as the Series 1 and Series 2 experiments. In each Series 3 test, the same pre-compaction and swelling stress measurement procedures were also followed as those used for the Series 1 and 2 tests, the only difference being that Ar was used as

pore fluid instead of CO_2. In Series 3, however, when the sample tested reached equilibrium during the swelling stress test stage (indicated by no further increase in axial load with time), the Instron was switched from position control to load control mode, and the axial load was then cycled through two or three cycles between the maximum and minimum axial stresses applied during the Series 1 and Series 2 swelling stress tests. Upon completion of two or three cyclic loading runs, the experiment was then terminated by unloading the sample, depressurizing the Ar and disassembly.

2.5. Calibrations and corrections

In making all swelling stress measurements, the samples were loaded in fixed Instron position mode with the result that pressurization of the Remanit oedometer vessel with fluid, whether CO_2 or Ar, led to (a) an increase in the axial load monitored by Instron load cell, accompanied and moderated by (b) a minor elastic deformation of the apparatus measured at the external LVDT (including elastic shortening of the Remanit and Ti loading pistons and expansion of the Remanit vessel), see Appendix A (Supplementary Material). Alongside these machine responses, introduction of fluid pressure during each swelling stress experiment reduced the axial effective stress supported by the sample, causing poro-elastic expansion of the sample, independently of any sorption-related swelling effect. Several calibration tests were done to determine the dependence of the Instron load cell and external LVDT signals upon fluid pressure by pressurizing the compaction vessel with CO_2 in the axially loaded condition, with the Instron position fixed and with no sample present in the Ti sample vessel. Linear best fits to the data obtained allowed the benchmark apparatus response, i.e. effects (a) and (b), to be quantified (see Appendix B, Supplementary Material). For each swelling stress experiment started at a pre-chosen effective stress σ_{start}, the initial effective axial stress (σ_e^{in}) supported by the sample immediately after CO_2 introduction, but before any sorption-induced swelling effect had occurred, could be calculated after correcting the axial force applied for effect (a). The swelling stress developed (i.e. measured change in Terzaghi effective stress) as a function of time following CO_2 introduction was computed from the measured load signal in the same way (see Appendix C, Supplementary Material). The stress evolution occurring in the control experiments performed using Ar was also calculated using this method, yielding the swelling stress produced by purely poro-elastic sample expansion (assuming zero or negligible swelling duo to Ar adsorption). The maximum error in applying these corrections to obtain the axial effective stress at any instant in any of our experiments was calculated to be 0.43 MPa.

Independently of the above machine effects caused by fluid pressurization, the development of swelling forces in our experiments inevitably caused elastic deformation of the loading system. This effect in turn allowed the loaded samples producing a swelling stress to undergo minor swelling strains even when the position of the loading piston was externally fixed. Careful calibration runs were performed to determine this elastic machine deformation, through axially loading and unloading the empty titanium sample vessel at conditions identical to those used in our swelling stress experiments, i.e. at 44° C and 10 MPa CO_2 pressure. A machine deformation correction was accordingly established, based on a fourth order polynomial fit to the external LVDT versus applied load data obtained (see Appendix A, Supplementary Material). The small sample strains that accompanied swelling stress changes could hence be obtained from the displacement data measured using the external LVDT, by correcting for machine deformation associated with changes in both axial load (i.e. swelling force changes) and applied fluid pressure (effect b above), see Appendix C (Supplementary Material). Sample swelling deformations occurring in the Ar control experiments of Series 3 were also computed using this method. The same correction procedure was likewise applied to the external LVDT signals obtained in the cyclic loading part of the Series 3 tests, yielding the change in thickness of the loaded sample versus axial load. This made it possible to determine the uniaxial elastic stiffness of the Series 3 samples from a linear fit to a plot of the reversible change in sample thickness versus applied load (see Appendix D, Supplementary Material).

Very precise external displacement measurements and calibrations are required to measure accurately the very small changes in sample dimensions discussed above. The external LVDT employed in our first series of experiments (S1 series, Table 1) was insufficiently accurate and showed too much hysteresis to enable sample strains associated with swelling stress development or minor CO_2 pressure fluctuations to be resolved adequately. We therefore present results on swelling deformation only for the S2 and S3 series of experiments. For these experiments, the maximum error in the correction for the machine deformation obtained, hence the maximum error in measuring changes in the sample thickness was ± 0.001 mm (i.e. ± 1 μm).

3. Results

3.1. Initial effective stress after CO_2 introduction

The initial effective normal stress σ_e^{in} resulting from the introduction of CO_2 into our apparatus at a pressure of 10 MPa, as calculated from our machine calibration data independently of any swelling/shrinkage effects in the sample, is presented for each clay experiment in Table 1. The equivalent (simulated) burial depth for each sample (Table 1) was calculated assuming a sedimentary rock column with an average density of 2250 kg/m^{-3} and the presence of a hydrostatic pore fluid pressure gradient. The difference between the pre-applied axial stress (σ_{start}) and the initial effective axial stress (σ_e^{in}), which represents the change in effective stresses ($\Delta\sigma^e$) supported by the sample upon CO_2 or Ar introduction, is given for each experiment in Table 1. We emphasise that these effective stress changes are induced by pore fluid pressurization and the associated machine deformation. The magnitude of these changes is around 15–17 MPa. This value varies from sample to sample due to minor variations in the pore fluid pressure employed in each experiment and to the uncertainties in our calibrations.

3.2. Swelling stress data – Series 1 experiments

In the first series of five experiments, three Na-SWy-1 samples, S1-M1 to S1-M3, were tested at pre-determined normal stresses (σ_{start}) of 27.2, 34.2 and 39.7 MPa respectively. The influence of a different smectite type (Ca-SAz-1) on stress development was studied in experiment S1-M4 (σ_{start} = 34.6 MPa), while experiment S1-M5 addressed the smectite-bearing shale (σ_{start} = 40.9 MPa, refer Table 1).

The raw data typically obtained in these experiments are illustrated in Fig. 2a. This shows the change in axial force and LVDT position signals, measured relative to their values at the start of experiment S1-M1, versus elapsed experimental time, as well as the same signals obtained in a calibration test performed at similar starting axial force (effective stress) but with no sample present. It is seen from Fig. 2a that the axial load and LVDT position values increase instantly upon introduction of CO_2 pressure in the calibration test, reflecting the elastic response of the machine upon fluid pressurization (an increase in LVDT signal means expansion). By contrast, in the swelling stress test on clay sample S1-M1, much larger instantaneous changes in axial load and LVDT position were measured upon CO_2 introduction at 10 MPa, as well as subsequent time-dependent development towards asymptotic plateau values. This behaviour clearly demonstrates a swelling effect and associated swelling stress development in the clay sample due to CO_2 introduction. Note that the excess axial force (stress) change measured in the test on sample S1-M1, relative to the calibration test, represents a total swelling force. The change in Terzaghi effective stress determined from this swelling force gives the 'swelling stress' reported in present paper and includes both poroelastic and any CO_2 uptake-induced expansion effects occurring in the sample.

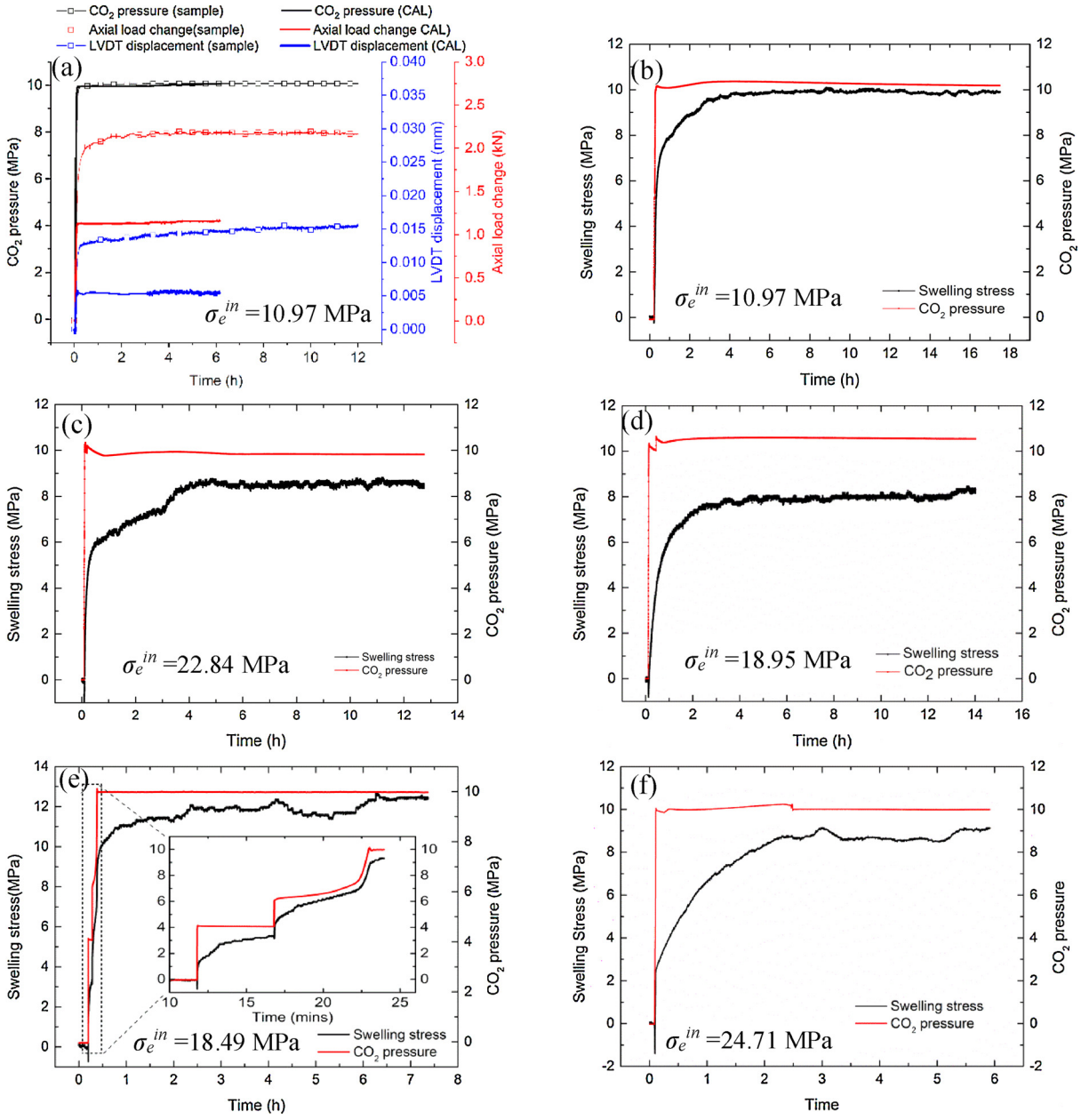

Fig. 2. Representative raw data and swelling stress vs. time plots for the Series 1 experiments. (a) Change in axial force and LVDT signal measured in experiment on S1-M1 vs calibration test with no sample present. Both tests were performed at a starting axial force of ~3.2 kN, equivalent to an initial effective normal stress of ~11 MPa. 'Sample' in the bracket denotes data for swelling stress test S1-M1, whereas 'CAL' denotes the calibration test with no sample present. (b) S1-M1, Na-SWy-1 material, initial effective normal stress σ_e^{in} is 10.97 MPa, simulated burial depth ~ 0.88 km. (c) S1-M2, Na-SWy-1 material, σ_e^{in} = 18.95 MPa, simulated burial depth ~ 1.52 km. (d) S1-M3, Na-SWy-1 material, σ_e^{in} = 22.84 MPa, simulated burial depth ~ 1.83 km. (e) S1-M4 on Arizona Ca-SAz-1 montmorillonite, σ_e^{in} = 18.49 MPa, simulated burial depth ~ 1.48 km. (f) S1-M5 on a natural, smectite-rich shale. σ_e^{in} = 24.71 MPa, simulated burial depth ~ 1.98 km.

The swelling stress data determined from experiments M1 to M3, after correcting for all machine effects and for changing CO_2 pressures during CO_2 introduction, are presented in Fig. 2b,c,d. These plots also show the history of CO_2 pressurization per test. In all cases, it is observed that when CO_2 is injected into the samples, a small negative swelling stress was measured for a short time period (less than one minute), before positive stresses were recorded, as the target CO_2 pressure of 10 MPa was reached. This was presumably due to transient compaction of the sample outweighing the swelling effect before the CO_2 had pervasively accessed the sample porosity.

Examining the three tests performed in series S1 on Na-SWy-1, we note that, upon increasing the initial effective normal stress σ_e^{in}, i.e. going from experiment M1 to M3, the swelling stress decreases in magnitude. By contrast, the rate of stress development varies slightly but shows no apparent correlation with the initial effective normal stress. For each individual test, once the target CO_2 pressure of 10 MPa is reached, a change in the rate of development of swelling stress is observed (Fig. 2b–d), beyond which the swelling stress continues to increase more slowly until it approaches stable value (i.e. an apparent equilibrium state) after an interaction time of ~4 h. The equilibrium swelling stresses (σ_{sw}), derived by averaging the swelling stress measured in the last 0.5–2 h of each individual test, depending on noise level, attained values around 10.0 MPa, 8.6 MPa and 8.0 MPa for M1 to M3 respectively, pointing to a decreasing trend in equilibrium value with increasing initial effective normal stress for Na-SWy-1 samples i.e. for σ_e^{in} values of respectively 11.0, 18.5 and 22.8 MPa corresponding to

equivalent burial depths of 0.88, 1.52 and 1.83 km – see Table 1.

The results of experiment M4 (Fig. 2e) on Arizona montmorillonite (Ca-SAz-1, σ_e^{in} = 18.49 MPa, equivalent burial depth 1.48km – Table 1) show similar swelling stress vs. time behaviour to that observed for Na-SWy-1 (M1-M3). When CO_2 was injected into the sample, a negative swelling stress was measured, suggesting transient compaction due to pressurization. Subsequently, after ~1 min, the swelling stress recovered back to values above zero, following similar behaviour to that measured for samples S1 M1-M3 during the further course of the experiment. From the point where the target pressure of 10 MPa was reached and kept constant henceforth, the swelling stress steadily increased to approach an apparent asymptotic equilibrium value (σ_{sw}) of ~12.4 MPa.

The results of the CO_2 experiment conducted with smectite-bearing shale are displayed in Fig. 2f. The basic characteristics of this plot are similar to those obtained for experiments M1 to M4, and show that the shale containing 53% smectite develops a swelling stress (σ_{sw}) of 9.3 MPa at conditions corresponding to an initial effective normal stress σ_e^{in} of 24.7 MPa and relatively deep simulated burial depths of almost 2 km (Table 1).

3.3. Swelling stress data – Series 2 experiments

To investigate the effect of the initial axial effective stress σ_e^{in} (i.e. simulated burial depth or overburden pressure) on the magnitude of axial swelling stress measured in each sample upon CO_2 introduction, the second series of five experiments were performed on Na-SWy-1 samples under a range of σ_e^{in} values (9.63–22.36 MPa), selected (via the choice of σ_{start}) to complement those employed in the three tests on Na-SWy-1 material reported in series S1 (10.97–22.84 MPa – see Table 1). Fig. 3a–h show the swelling stress development with time measured for the S2-M6 to M13 samples. Most of the S2 experiments were allowed to run for more than the 6 h employed in the S1 tests, allowing (apparent) equilibrium to be more closely approached (see Fig. 3). We found that the swelling stresses approached their asymptotic equilibrium value within ~4 h, as in the S1 runs, the only exception being sample S2-M8 (Fig. 3c) which developed an extra 1 MPa swelling stress between 4 and 12 h. By taking the average value of the swelling stress measured in the last one to two hours of each run, we determined the magnitude of equilibrium swelling stresses (σ_{sw}) in each of the Series 2 experiments. These values decrease systematically from 10.8 to 7.0 MPa as the initial effective axial stress applied to the sample increases form 9.6 MPa to 22.9 MPa. This decreasing trend is similar to that observed for M1-M3 in Series 1 (see Fig. 3 and Table 1).

Results on equilibrium swelling stress (σ_{sw}) and final effective axial stress supported by sample at equilibrium ($\sigma_e^{eq} = \sigma_e^{in} + \sigma_{sw}$), derived from the swelling stress vs. time curves obtained for the Series 1 and Series 2 experiments, are presented in Table 1. The complete set of data for Na-SWy-1 samples show a clear effect of increasing initial effective stress σ_e^{in}, and final (equilibrium) effective stress σ_e^{eq}, on the extent of swelling stress development in Na-SWy-1 smectite due to exposure to CO_2 – see Fig. 4a and b respectively. These plots show similar trends for both series of experiments on Na-SWy-1 samples, with swelling stress decreasing almost linearly with increasing initial and final effective stress. The sensitivity of swelling stress (σ_{sw}) to final or equilibrium axial stress was determined for the combined S1 and S2 data sets by linear best fitting (see Fig. 4b), which yielded the relation

$$\sigma_{sw}^{eq} = -0.281\sigma_e^{eq} + 16.021 \quad (1)$$

This of course means that if the effective axial stress experienced by a Na-SWy-1 sample at equilibrium increases by 1 MPa, the swelling stress developed decreases by ~0.28 MPa.

As discussed in Section 2.5, even though the piston position was fixed during each experiment, any swelling stress development in the sample inevitably led to elastic deformation of the loading system, resulting in a small change in sample thickness, i.e. to an absolute sample swelling, x_{sw}. The high precision LVDT employed in the apparatus used for the Series 2 experiments, allowed this minute swelling deformation to be determined for samples M6-M13 at any instant, by correcting measured displacement for machine response to axial load and any changes in fluid pressure. The swelling deformations occurring in the S2 samples at equilibrium are presented in Table 1 in terms of absolute thickness increase, and are plotted versus corresponding equilibrium swelling stress σ_{sw} in Fig. 5. This plot clearly shows that the swelling of the sample, hence the displacement of the upper titanium piston interface with the sample relative to the lower titanium piston interface, is linearly proportional to the equilibrium swelling stress, reflecting that the elastic deformation of the machine, which accommodates sample swelling and is equal and opposite to it, is directly proportional to the equilibrium swelling stress via the machine stiffness constant.

3.4. Results of the Series 3 control tests performed using Ar

The Series 3 experiments on Na-SWy-1 montmorillonite involved equilibration with 10 MPa Ar in a manner identical to the Series 2 and 3 swelling experiments performed with CO_2, followed by cycling of the axial load, hence effective axial stress, to cover the full range of swelling stresses encountered in the Series 2 and 3 tests. The initial equilibration stage of these swelling stress experiments led to the development of an apparent swelling stress in a manner closely similar to that seen using CO_2 (cf. the Series 1 and 2 tests in Figs. 2 and 4), but with a magnitude of only 2–3 MPa instead of 7–12 MPa (Table 1 and Fig. 4A). Representative results of the subsequent load cycling tests are as shown in Fig. 6 (2 loading and unloading cycles for sample S3-M2). The total deformation of the sample and Remanit/Ti loading pistons, measured at the external LVDT, during load cycling is plotted against uniaxial load applied in Fig. 6, along with the apparatus deformation derived from the fourth order polynomial calibration described above, and with the inferred sample deformation (the difference). Linear fitting to the piston distortion and sample deformation versus axial load data demonstrates closely linear behaviour (dashed lines in Fig. 6), and yields compliance coefficients of respectively 0.00837 kN/mm for the machine and 0.00144 mm/kN for the sample, equivalent to apparent stiffness moduli of ~119 kN/mm and 694 kN/mm. Several such tests were performed in the Series 3 experiments, yielding an average sample stiffness of 538 kN/mm.

4. Discussion

4.1. Swelling stress development in the presence of CO_2: phenomenology and mechanism

Our experiments on Na-SWy-1, Ca-SAz-1 and smectite bearing shale show that exposure to supercritical CO_2, under the confined conditions imposable in the apparatus used, produces swelling stresses of significant magnitude (7.0–12.4 MPa) at (apparent) equilibrium. The swelling stresses developed in Na-SWy-1 smectites in experimental series S1 and S2 are in good agreement, with a clear negative dependence on initial effective stress (σ_e^{in}), i.e. on the simulated burial or overburden stress, and on the final effective stress (σ_e^{eq}) at equilibrium (Fig. 4). The machine stiffness/compliance effects described above mean that loaded samples producing a swelling stress can undergo small swelling strains when the CO_2 pressure increases or when swelling stress develops. Taking into account the combined axial stiffness of our apparatus (119N/mm) plus the samples (538 kN/mm, corresponding to 4.64G Pa/mm), the magnitude of the swelling stress measured in our Series 1 and Series 2 experiments is consistent with the swelling strains of a few percent observed in experiments on mechanically unconfined samples performed on similar clays and under otherwise similar conditions (De Jong et al., 2014; Giesting et al., 2012a,b; Ilton et al., 2012; Schaef et al., 2012).

When analyzing our data on swelling stress development upon

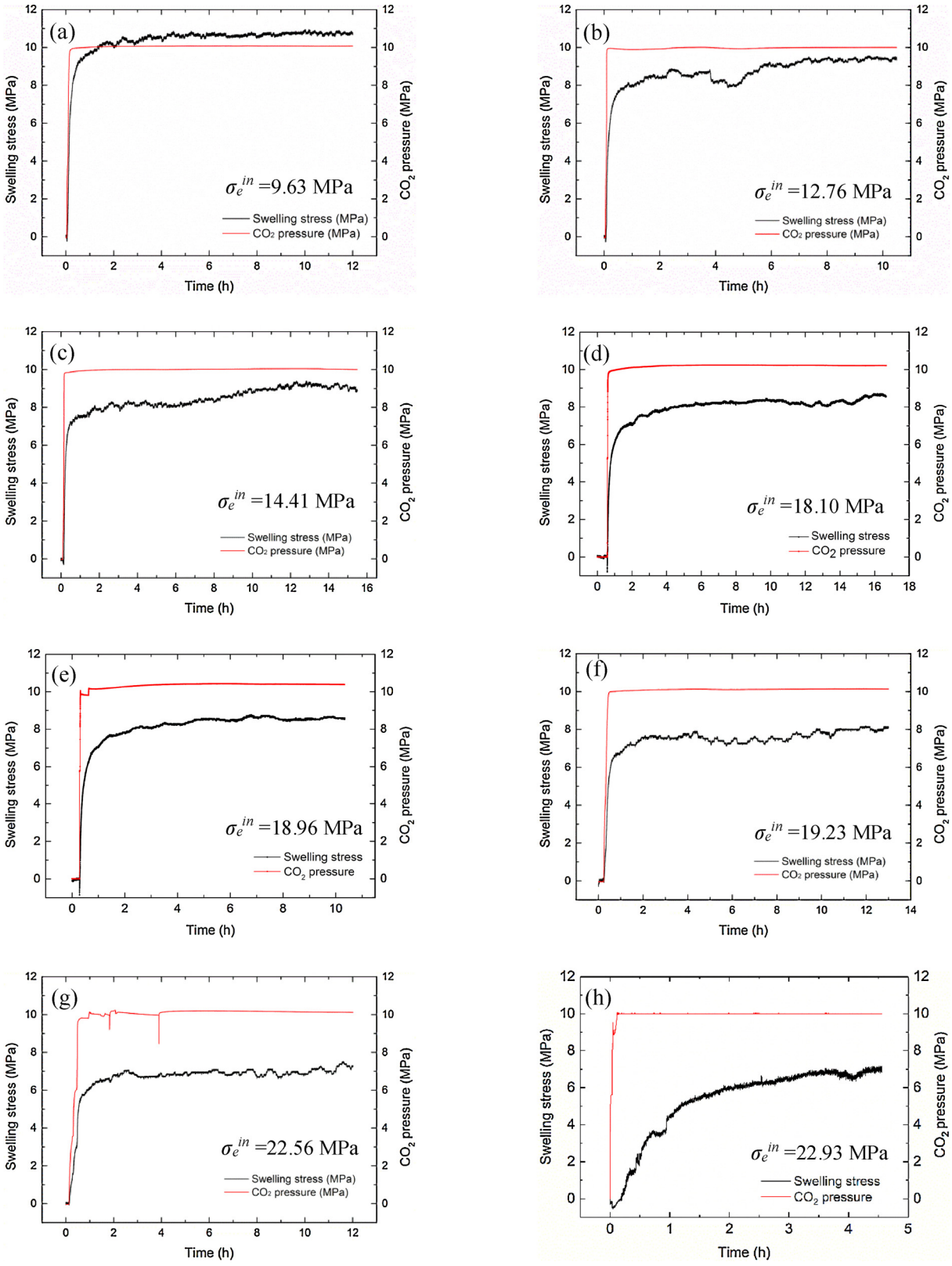

Fig. 3. Swelling stress development due to exposure to CO_2 measured in the Series 2 experiments on Na-SWy-1 material. (a) Sample M6 subjected to initial effective normal stress (σ_e^{in}) of 9.63 MPa, simulated burial depth is ~0.77 km. (b) Sample M7, σ_e^{in} = 12.76 MPa, simulated burial depth is ~1.02 km. (c) Sample M8, σ_e^{in} = 14.41 MPa, simulated burial depth is ~1.15 km. (d) Sample M9, σ_e^{in} = 18.10 MPa, simulated burial depth is ~1.45 km. (e) Sample M10, σ_e^{in} = 18.96 MPa, simulated burial depth is ~1.52 km. (f) M11, σ_e^{in} = 19.23 MPa, simulated burial depth ~1.54 km. g) M12, σ_e^{in} = 22.56 MPa, simulated burial depth ~1.80 km. (h) M13, σ_e^{in} = 22.93 MPa, burial depth ~1.83 km.

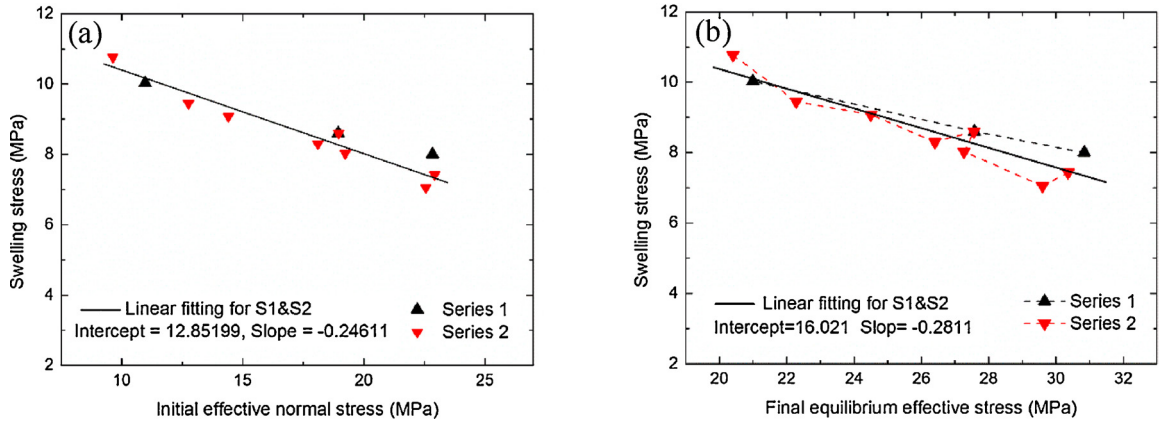

Fig. 4. (Apparent) equilibrium swelling stress (σ_{sw}) plotted against (a) initial effective axial stress (σ_e^{in}) for Na-SWy-1 samples (i.e. Series S1: M1 to M3 and Series S2: M6 ~ M13) at $P_{CO2} \approx 10$ MPa, and (b) final effective normal stress (σ_e^{eq}) experienced by each sample at equilibrium with 10 MPa CO_2.

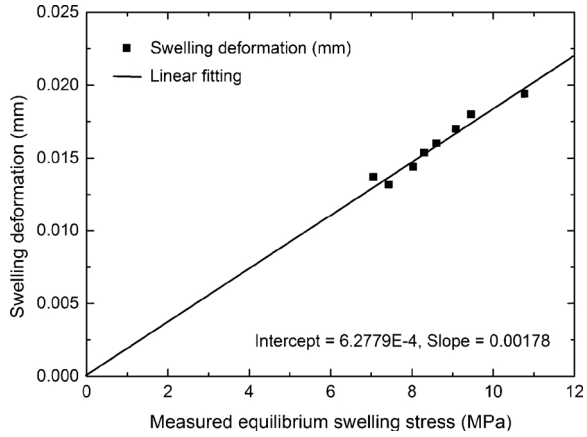

Fig. 5. Absolute swelling deformation (x_{sw}) plotted versus corresponding swelling stress (σ_{sw}) for the second series of experiments (samples S2-M6 to M13). The stresses and displacements were measured at (apparent) equilibrium with a CO_2 pressure of 10 MPa.

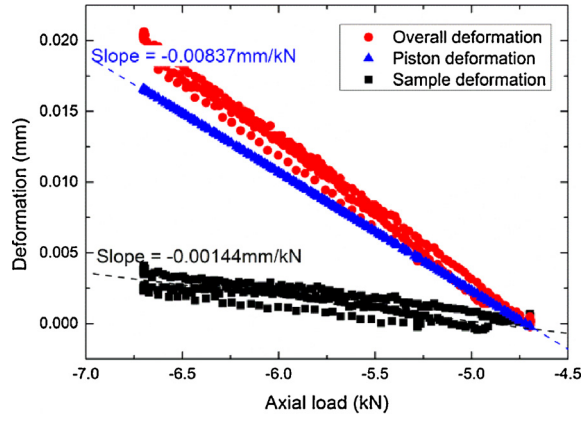

Fig. 6. Representative results of the Series 3 load cycling tests performed on Na-SWy-1 samples at an Argon pore fluid pressure of 10 MPa. Total deformation measured by external LVDT, deformation of the apparatus (mainly Remanit pistons), and deformation of the sample are plotted against uniaxial load applied for S3-M2. Linear fitting of the sample deformation vs. axial load gives a value of 0.00144 mm/kN for the compliance coefficient of the sample.

exposure to CO_2 in more detail, the results for Na-SWy-1 show that samples subjected to higher initial effective stress σ_e^{in} (e.g. S1-M3, Fig. 2d), not only show lower equilibrium swelling stress values, but also lower rates of swelling stress development (cf. S1-M1, Fig. 2b). These findings qualitatively agree with the effects of applied stress on sorption of CO_2 by coal reported recently (Hol et al., 2011, 2012, 2014; Espinoza et al., 2014). They also agree with the predictions of thermodynamic models for the effects of stress state on sorption and on sorption-induced swelling presented by these authors for two-component sorbent-sorbate system such as coal plus CO_2 or CH_4. (see also Liu et al., 2015 and Liu et al., 2016).

While the thermodynamic models developed by Hol et al. (2011, 2012) and Liu et al. (2016) predict lower sorption capacities with increased effective stress, hence reduced swelling and therefore lower swelling stresses, we note that the clay-water-CO_2 system is much more complex than a two-component sorbent-sorbate system such as coal plus CO_2. Several additional effects could be important, in particular the role of hydration state and how this is affected by the presence of CO_2 (De Jong et al., 2014; Wentinck and Busch, 2017; Busch et al., 2016). The hydration state of the clays tested in our experiments is only constrained by the fact that the samples were allowed to equilibrate with laboratory humidity (RH 40–60% at T = 20–25 °C) at the experimental temperature of 44 °C prior to introduction of CO_2. Despite the fact that previous work (De Jong et al., 2014) implies a corresponding hydration state in the zero to 1 water layer range ($10.0 \leq d_{001} \leq 12.3$ Å), the exact initial hydration state in our experiments, and the extent to which this may change when CO_2 is injected into the sample, are not known. The exact effects of hydration state, especially in-situ hydration state, thus form an important target for future work on the effects of simulated burial stress (σ_e^{in}) on swelling stress and strain response.

Aside from the magnitude of swelling stress, the rapid rate of CO_2 uptake in the present confined experiments, evidenced by the fast development of swelling stress seen in Figs. 2 and 3, is also in good agreement with what has been observed previously in experiments on mechanically unconfined samples performed on thin Na-exchanged and K-exchanged Na-SWy-1 smectite films (Giesting et al., 2012a, 2012b – using XRD methods) and on mm-sized pressed cubes of Na-SWy-1 smectite clay (De Jong et al., 2014 – using optical strain measurements). In these experiments, the samples were in effect immersed in CO_2 leaving the clay free to swell against only the CO_2 pressure. Exposure to CO_2 caused swelling of several percent with the swelling occurring in a few minutes only. This behaviour was argued by Giesting et al. (2012a) to reflect rapid diffusion of CO_2 both into the clay samples and into the smectite interlayer region. However, the mode of interaction between CO_2 molecules, water molecules and interlayer cations in the interlayer space is not fully clear. Giesting et al. (2012a) speculate that the CO_2 and interlayer water molecules interact to form charged carbonate complexes (CO_3^{2-}/HCO_3^-) and interact electrostatically with the interlayer cations, causing changes in interlayer d-spacing. Indications supporting this theory were reported by Hur et al.

(2013) and Romanov (2013), while other authors present convincing arguments against the formation of carbonate complexes (see discussion by Busch et al., 2016). In broad alignment with the work of Hur et al. and Romanov, Loring et al. (2012–see also Rother et al., 2013; Giesting et al., 2012a,b) recently demonstrated direct intercalation of CO_2 into the Ca-, Na-, and K-smectite interlayer structure using neutron scattering and neutron magnetic resonance techniques. Moreover, Romanov (2013), on the basis of measurements made using attenuated total reflection infrared spectroscopy, argued formation of (amorphous) carbonate species in the interlayer spaces of SWy-2 and STx-1b smectites exposed to CO_2, suggesting permanent trapping of CO_2 by the smectites investigated. However, Loring et al. (2012) and Schaef et al. (2012) argued against this point of view, respectively through thermogravimetric measurements and magic angle spinning nuclear magnetic resonance spectroscopy on Ca-STx-1 montmorillonite. In summary, the mechanisms leading to clay swelling in the presence of CO_2 and water remain a field for further study.

In the present Series 1 and 2 experiments, we observed that the swelling stress developed in Ca-SAz-1 material is significantly higher than in Na-SWy-1 subjected to similar normal effective stress (experiments S1-M4 vs. S1-M2, S2-9 & S-210). Specifically, the 12.4 MPa swelling stress produced in experiment S1-M4 on Ca-SAz-1 is 50% higher than the ~8 MPa measured for Na-SWy-1 under similar P-T, humidity and effective stress conditions (refer Table 1). This is nicely consistent with the similar difference in swelling magnitude reported by Giesting et al. (2012a,b), based on XRD measurements on Na^+ and Ca^{2+} exchanged SWy-2 montmorillonite exposed to similar fluid pressure and temperature conditions but unconfined, i.e. without an effective stress on the samples. Our results are also consistent with those of De Jong et al. (2014), who showed that Ca-montmorillonite (with an initial hydration state corresponding $d_{001} \approx 12.5$ Å) can develop maximum swelling strains up to ~15%, in comparison to Na-montmorillonite ($d_{001} \approx 11$ Å) which showed lower values of ~10%. Returning specifically to the study presented here, the discrepancy between Ca- and Na- montmorillonite probably reflects an initially higher hydration state in Ca-SAz-1 than in the Na-SWy-1 material (Bird, 1984; Sato et al., 1992), while at the same time the radius of Ca^{2+} is larger than Na^+ resulting in a larger interlayer spacing in the Ca-SAz-1 than Na-SWy-1 materials. These factors might allow easier access of CO_2 into the interlayer space. At present however, we can only speculate on the CO_2-cation-water interactions taking place in smectite interlayers.

The results of experiment S1-M5 on the shale sample containing ~53% smectite (Fig. 2e) show a swelling stress of ~9.3 MPa, despite a) the high effective stress (σ_n^e) conditions corresponding to a burial depth of ~2 km, and b) the fact that the smectite content of the shale was only 53%. No information is available on the structure or interlayer cation type(s) for this sample material. It is therefore difficult to make direct comparisons with the results obtained for Na-SWy-1 and Ca-SAz-1. The unexpectedly high swelling stress measured for the shale sample may be attributable to the type of smectite it contains. If the interlayer cation would be Ca^{2+} we can speculate that a swelling stress equal to half of that developed in pure Ca-SAz-1 should develop for the shale due to its ~53% smectite content, i.e. ~6.2 MPa. Further, the significant quartz content of the shale sample can be expected to impart a higher stiffness modulus, hence yielding a higher swelling stress. At the same time, we note that besides likely intercalation of CO_2 into the interlayer region of the smectite present in the shale sample, the relatively high swelling stress measured might also be related to clay-CO_2 interactions occurring at the external platelet surfaces (faces and edges) of other non-swelling clay minerals, such as illite and kaolinite (Busch et al., 2008). It is well-established that water films can easily adsorb on these charged surfaces due to the attraction exerted by exchangeable, charge-compensating surface cations (Rutter, 1983; Ormerod and Newman, 1983; Israelachvili et al., 1988; Renard and Ortoleva, 1997; Hatch et al., 2012). The properties of such surfaces might therefore not be very different from the smectite interlayer region, in terms of interaction with CO_2. Of course, similar effects might occur at the surface of smectite crystallites also, as speculated already by De Jong et al. (2014).

In Series 3 experiment performed using Ar as the pore fluid, we measured 2–3 MPa swelling stress accompanied with a swelling strain of less than 1%. The swelling stress and strain attained are much less than those measured in the Series 1 and 2 tests using CO_2 as pore fluid. In view of the fact that Ar is chemically inert, like He, and that the latter is reported not to cause interlayer swelling of smectite, we infer that the swelling stresses and swelling strains measured in the Ar tests reflect poro-elastic expansion of the clay samples, induced by the decrease in Terzaghi effective stress upon pressurization with Ar.

4.2. Swelling stress at zero sample strain

As discussed in relation to the S3 series of experiments on Na-SWy-1 material (Fig. 6), swelling stress development in our samples inevitably leads to elastic deformation of the loading system and sample, resulting in an accompanying small change in sample thickness, i.e. to an absolute sample swelling (x_{sw}) and associated swelling strain. This means that the swelling stress measured by our system will always be lower than the value that would be attained under conditions of zero apparatus distortion and zero sample strain, i.e. under conditions where axial swelling of the sample is fully restricted. The swelling stress at zero strain will, of course, be determined purely by the swelling and (poro)elastic properties of the sample, with the swelling strain produced by interaction with CO_2 being entirely accommodated by elastic compression of the sample. The implication is that the only truly meaningful way to express swelling stress, for a given sample material under given conditions, is in terms of the equilibrium swelling stress pertaining at zero strain. This will be the maximum swelling stress that the material can generate when fully equilibrated with CO_2, with all direct measurements of swelling stress yielding lower values by virtue of the fact that no machine (or natural confining environment) is infinitely stiff in practice.

In Appendices 5 and 6 (Supplementary Material), we derived how the measured swelling stress and swelling strain are related, and show how the measured swelling stress can be extrapolated to zero swelling strain, taking into account the dependence of swelling strain on applied effective stress. The required relationship is given by:

$$F_{sw}^{\in=0} = \frac{(1 - k_s \cdot c_1) F_{sw}^{eq} + k_s \cdot x_{sw}^{eq}}{1 - k_s \cdot c_1} \tag{2}$$

where $F_{sw}^{\in=0}$ is the swelling force attained while the measured equilibrium swelling deformation x_{sw}^{eq} is completely cancelled by elastic accommodation, F_{sw}^{eq} is the measured equilibrium swelling force, k_s is the average sample stiffness estimated to be 538 kN/mm, and $c_1 = -3.35$um/kN is the coefficient derived from Eq. (1), which shows how the adsorption induced swelling deformation decreases with increasing load applied to the sample (see Appendix E, Supplementary Material). The swelling stress extrapolated to 'zero' sample strain, $\sigma_{sw}^{\in=0}$, accordingly can be obtained from

$$\sigma_{sw}^{\in=0} = \frac{F_{sw}^{\in=0}}{A_s} = \frac{(1 - k_s \cdot c_1) F_{sw}^{eq} + k_s \cdot x_{sw}^{eq}}{(1 - k_s \cdot c_1) \cdot A_s} \tag{3}$$

where A_s is the cross section area of samples tested.

Substituting the apparent equilibrium sample swelling x_{sw} and swelling stress measured in each swelling stress test into the above equation, the swelling stresses developed at 'zero' strain can be obtained and are plotted in Fig. 7. The resulting values vary from 42.9-29.3 MPa over the range of 9–23 MPa initial normal effective stress, and thus decrease systematically with increasing simulated overburden stress as implied by the correlation given in Fig. 4. Note that the extrapolated swelling stress in this case was contributed not only by the swelling effect related to interlayer CO_2 uptake or sorption by the

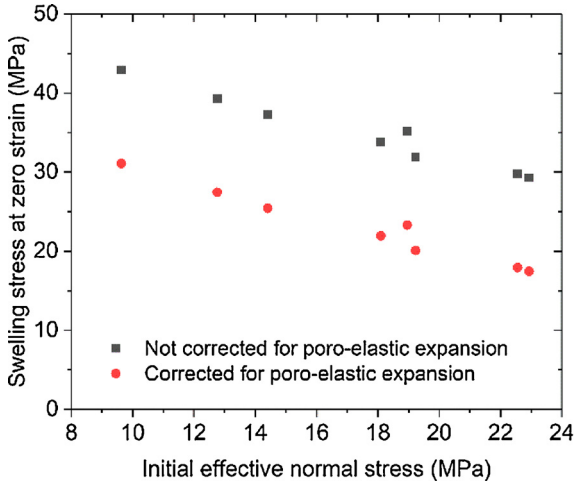

Fig. 7. Swelling stress extrapolated to "zero sample strain" conditions plotted as a function of initial effective stress for the second series of experiments (S2-M6 to S2-M13). The extrapolated swelling stress is the stress calculated to develop in the sample when the sample expansion due to CO_2-smectite interaction is fully restricted, i.e. where sample swelling strain is exactly offset by elastic compression of the sample. Black data points are the swelling stress required to cancel out the total swelling strain occurring in the experiments, not correcting for the poro-elastic effect. Red data points are the swelling stress needed to cancel out swelling related to CO_2 uptake by the sample only (i.e. excluding poro-elastic swelling related to effective stress change upon pressurization with CO_2). (For interpretation of the references to colour in this figure legend, the reader is referred to the web version of this article.)

smectite samples, but also by poro-elastic expansion of the sample due to the decrease in effective stress supported by the sample at the instant that the Remanit compaction vessel was pressurized with CO_2 at 10 MPa. The poro-elastic contribution was measured in our swelling stress tests using Ar (i.e. Series 3 experiment), and should be the same as that in tests using CO_2 as pore fluid, assuming that the truly elastic properties of the pre-compacted samples were not changed by interaction with Ar or CO_2. The contribution of the poro-elastic effect to the swelling stress and swelling strain measured in our CO_2 tests can be removed by subtracting the respective reference values measured in our Ar tests. The swelling stress at zero strain, produced solely by the uptake-induced swelling effect, can then be calculated by inserting the corrected sorption-induced swelling strain and swelling stress into Eq. (3). This yields swelling stresses due to interlayer CO_2 uptake/sorption of 17.5-31.1 MPa (Fig. 7, solid red circles).

4.3. Implications for geological storage of CO_2

We have demonstrated that Na-SWy-1 and Ca-SAz-1smectite clays and crushed smectite-bearing shale develop a swelling stress when exposed to (supercritical) CO_2 under laterally confined conditions characterized by an initial vertical effective stress and a temperature typical of carbon sequestration sites (up to 2 km burial depth). The experiments were conducted under temperature-humidity conditions that are expected, from previous work (Giesting et al., 2012a,b; De Jong et al., 2014) to produce a hydration state in the range 0–1 water layer for Na-SWy-1 and 1–2 water layers for Ca-SAz-1 smectite. This hydration state is also expected to be representative for *in-situ* reservoir and caprock conditions at depths up to 2–3 km (Bird, 1984). The magnitude of the directly measured swelling stress was found to be of the order of 7.0–12.4 MPa for CO_2 pressures of 10 MPa and simulated burial depths of 0.8–2.0 km. Control experiments using Argon instead of CO_2 show that these values include a contribution of 2–3 MPa due to poro-elastic expansion of the samples caused by the decrease in Terzaghi effective stress that accompanies pressurization with CO_2. In addition, the measured swelling stress values are in part determined by elastic deformation of the apparatus used to measure them. Making use of our data to remove this effect, i.e. to extrapolate our data to a condition where the sample is constrained such that all swelling strain is accommodated by elastic deformation of the sample, with zero strain, demonstrates that swelling stresses then reach values of 29.3–42.9 MPa. After removing the poro-elastic effect induced by pressurization with CO_2 to 10 MPa reduces these values to swelling stresses of 17.5–31.1 MPa. These results, coupled with the swelling strains that we measured previously under similar conditions in unconfined experiments on similar material (De Jong et al., 2014), suggest that penetration of CO_2 into smectite-rich caprocks and fault gouges at CO_2 storage sites should lead to a local swelling/self-stressing effect, developing strains of several percent where nearly free to swell, or else normal stresses potentially of several to a few tens of MPa depending on the rock volume penetrated and the stiffness of the surrounding rock mass. (c.f. Wentinck and Busch, 2017). Shear stresses of similar magnitude might also potentially be generated due to heterogeneous and/or anisotropic swelling induced by CO_2 penetration. This type of swelling/self-stressing effect has not yet been accounted for in evaluating storage system integrity. On the other hand, it is important to realize that water-scavenging by dry, injected CO_2 might change the hydration state of smectites present in reservoirs, caprocks and faults, possibly even producing dehydration-related shrinkage (Gaus et al., 2005; Espinoza and Santamarina, 2012). Such CO_2-induced dehydration and shrinkage effects have been reported recently for swelling clays having two or more hydration layers (Schaef et al., 2012). According to Bird (1984), however, this hydration state is more likely relevant at low effective stress conditions (close to surface, potentially in faults), while at depths relevant for CO_2 storage ($>$ 1000 m) fewer than two hydration layers can be expected, depending on the interlayer cation and subsurface conditions. The competing effects of both water and CO_2, therefore need careful consideration. Moreover, while it is assumed that the (initial) 0–1 water layer hydration state investigated here is representative for *in-situ* conditions, direct evidence for this (e.g. Bird, 1984) is sparse and needs to be confirmed.

Taking the present results, along with those reported in our work on unconfined swelling (De Jong et al., 2014), as being applicable to *in-situ* conditions, clay swelling caused by CO_2 intercalation into the smectite interlayer region, is potentially capable of causing significant permeability reduction in reservoirs, caprocks and faults, due to closure of pores, cracks and void space and associated self-stressing. This would suggest that if CO_2 migrates slowly into joints or pores in a smectite-bearing shale caprock, for example, then swelling could impede migration and improve the caprock sealing properties. The magnitudes of the swelling stresses measured under confined conditions in the present study indicate that pore/fracture "closure stresses" (i.e. normal stresses) up to several tens of MPa can potentially be generated.

At the same time, sorption-induced stresses developing under 1-D strain or other geometrically constrained conditions, can promote the development of anisotropic states of stress, i.e. shear stresses, potentially causing damage or even failure (c.f. coal failure; Espinoza et al., 2015). The magnitude of the swelling stresses obtained here could be disadvantageous if they develop in regions where high deviatoric (shear) stresses already exist as a result of tectonic strains or the pressure and/or temperature changes associated with CO_2 injection. Examples of such sites include zones where sealing faults cut reservoir and caprock units, and where pressure changes in the reservoir can accordingly produce substantial shear stresses on the fault (Orlic et al., 2011). In such situations, and in situations where faults are already critically stress due to the background tectonic stress field (Zoback, 1992; Sperner et al., 2003), additional CO_2-induced swelling of smectites in the caprock could potentially lead to fault reactivation, or to local (non-uniform) caprock swelling and damage, and thus the creation of CO_2 leakage paths (Wentinck and Busch, 2017). At the same time, swelling of clays in the fault might increase the effective normal stress on the fault sufficiently to stabilize the fault. The present data

provide a basis upon which the potential role of such effects can be assessed in future.

Overall, however, by comparison with the effects that CO_2-induced swelling has on the in-situ transport properties and fracturing behaviour of coal beds (Hol et al., 2011, 2012), we do not expect that smectite swelling due to CO_2 uptake is likely to impair CO_2 storage system integrity significantly. Rather, as reported for CO_2-induced swelling of coal (Hol et al., 2012), the dominant effect is likely to be that normal stresses will increase due to swelling, which will close cracks present and stabilize faults. To assess if this is indeed the case, numerical modelling of the site specific *in-situ* state of stress, and the way it evolves, is required to evaluate the potential for CO_2-induced caprock damage or enhanced sealing via smectite swelling. In addition, further research is needed to investigate more systematically the range of swelling stresses that could develop from interactions with CO_2, for various pure smectite compositions, and especially for true *in-situ* hydration states – namely at *in situ* pressure and temperature conditions buffered by the presence of liquid water. It is also important to establish whether water scavenging by CO_2 can dry out smectites present in top seals and faults under *in-situ* conditions, as this would tend to reduce effective normal stresses and to open cracks, thereby reducing seal integrity (see discussion in Busch et al., 2016). As discussed above such dry-out (shrinkage) of interlayers in the presence of dry CO_2 was observed by Schaef et al. (2012, 2015) when the initial hydration state was 2 or more water layers.

In line with this, further research is also required on the swelling and self-stressing behaviour of natural caprock and fault rock materials containing both smectites and non-swelling clays, such as kaolinite and illite. Illite usually is the dominant clay phase at depths beyond 3 km. As discussed above, it is possible that the external crystallite surfaces of both smectites and minerals such as illite and kaolinite may exhibit CO_2 sorption effects causing swelling. These could play a role in caprocks and faults at depths up to and beyond 2–3 km, and need to be assessed.

5. Conclusions

In this study, we conducted laterally constrained, axi-symmetric compression experiments on pre-pressed discs of pure smectite (Na-SWy-1 and Ca-SAz-1 montmorillonite) clays, and on a smectite-bearing shale (53% smectite), to investigate the development of axial swelling stress due to exposure of the samples to SC CO_2 under mechanically confined conditions. The experiments were carried out at a nominal temperature of 44 °C, to ensure that the initial hydration state of the smectites would correspond to expected *in-situ* ranges (between respectively zero and one versus one and two planes of interlayer water molecules, for the Na-SWy-1 and Ca-SAz-1 montmorillonite). The CO_2 pressure used was 10 MPa. Vertical effective stresses up to 24.7 MPa were imposed, to simulate effective overburden stresses upon injection, corresponding to burial depths up to almost ~2.0 km. Three individual experiments were performed on Na-SWy-1 smectite samples as the control group, using Ar at 10 MPa as the pore fluid phase. The following conclusions were drawn:

1. Na-SWy-1 and Ca-SAz-1 montmorillonites and smectite-bearing shale (53% smectite) show the development of significant swelling stress as a result of exposure to SC CO_2 under mechanically confined conditions. In contrast, control experiments performed on Na-SWy-1 montmorillonite using Ar, exhibit limited swelling stress (2–3 MPa) due to poro-elastic expansion of the samples. The larger effect of CO_2 reflects intercalation of CO_2 molecules into the interlayer structure of smectite and possibly effects of clay surface sorption too. The maximum effective swelling stress attained under the present conditions, including poro-elastic effects, was almost 11 MPa for Na-SWy-1 clay at an initial effective stress simulating a burial depth of ~0.8 km. When extrapolated to zero sample swelling strain (at which point swelling is exactly accommodated by compressive elastic deformation of the samples), the swelling stresses predicted reach values of up to 43 MPa. These results indicate that CO_2-induced swelling and self-stressing can be expected to occur and are significant at *in-situ* conditions corresponding to 0.8-2.0 km of burial.
2. The CO_2-induced swelling stress produced in Na-SWy-1 montmorillonite decreases with increasing effective stress, or simulated burial depth, to a magnitude of ~7.0 MPa for a simulated depth of ~1.83 km (effective stress of 22.93 MPa). This effect, and the overall self-stressing behaviour observed over and above the poro-elastic effect, are qualitatively consistent with recent thermodynamic models (e.g. by Hol et al., 2012 and Liu et al., 2016) describing the coupled stress-strain-sorption behaviour of solids that swell when a sorbate is taken up into their structure.
3. The Ca-SAz-1 smectite samples investigated in present study developed significantly (50%) higher swelling stress than the Na-SWy-1 samples under similar P-T, humidity and effective stress conditions. We speculate that this is related to the lager interlayer spacing of Ca-SAz-1 versus Na-SWy-1 montmorillonite, which results from a higher initial hydration state at the lab RH condition and larger interlayer cation Ca^{2+}. Together, these may allow more CO_2 molecules to be uptaken into the interlayer space and hence retained there.
4. In view of its limited smectite content (53%), the smectite-bearing shale developed unexpectedly high swelling stresses upon exposure to CO_2 under the same conditions used in the experiments on Na-SWy-1 and Ca- SAz-1 smectites, generating ~9.3 MPa for a simulated burial depth of almost 2.0 km. This may reflect (a) the higher stiffness of the smectite shale, resulting from the presence of stiff minerals such as quartz, (b) the intrinsic interlayer properties and hydration state of the smectite phase(s) present, (c) the possibility of a swelling stress being produced by CO_2 uptake on the surface of non-swelling clay mineral constituents, such as illite and kaolinite. These possibilities require further investigation.
5. The swelling stresses measured under confined conditions in the present study are qualitatively consistent with expectations based on the swelling strains of several percent measured previously on the same materials under unconfined conditions (e.g. De Jong et al., 2014) and on the stiffness of the present experimental set-up. Taken together, the results suggest that penetration of smectite-bearing caprocks or fault rocks by CO_2, at CO_2 storage sites, will tend to produce local swelling and self-stressing behaviour, increasing normal stresses to close cracks and improve sealing capacity rather than degrading it. However, there is also a possibility that swelling-induced shear stresses could promote fault reactivation and damage development, and that water scavenging by dry CO_2 could dehydrate wet smectites to cause shrinkage and crack opening. To confirm/evaluate these possibilities, further experimental research (e.g. flow through experiment on smectite bearing carprock materials using dry and/or wet CO_2 as flowing fluid) and numerical modelling research are needed.
6. The present experiments have focused on smectite hydration states in equilibrium with atmospheric moisture (T = 20–25 °C, RH = 40–60%) at a nominal temperature of 44 °C, as this state (0–1 water interlayers in Na-SWy-1 smectite, 1–2 water interlayers in Ca-SAz-1 smectite) is believed to be achieved under *in-situ* conditions corresponding to 1–2 or perhaps 3 km depth. Future work should confirm that the assumed hydration states are indeed the hydration states under *in-situ* conditions, and the observed swelling stress effect would indeed occur under reservoir conditions. This can be done by investigating swelling and self-stressing behaviour under *in-situ* conditions and at various relative humidity, including that buffered by the presence of liquid pore water.

Acknowledgements

This study was performed within the Dutch National Carbon Capture and Storage Research Programme (CATO-2) under direct funding by Shell Global Solutions International B.V. (Contract GFSTE1101186, Amendment PT12793). The China Scholarship Council (CSC) is acknowledged for financial support granted to the first author Zhang. We also thank Colin Peach, Suzanne Hangx, Pieter Bertier, Tim Wolterbeek and Jinfeng Liu for fruitful discussions and for their advice on laboratory methods.

References

Bird, P., 1984. Hydration-phase diagrams and friction of montmorillonite under laboratory and geologic conditions, with implications for shale compaction, slope stability, and strength of fault gouge. Tectonophysics 107, 235–260.

Bishop, J.L., Pieters, C.M., Edwards, J.Q., 1994. Infrared spectroscopy analyses on the nature of water in montmorillonite. Clays Clay Miner. 42 (6), 702–716.

Busch, A., Alles, S., Gensterblum, Y., Prinz, D., Dewhurst, D.N., Raven, M.D., Stanjek, H., Krooss, B.M., 2008. Carbon dioxide storage potential of shales. Int. J. Greenh. Gas Control 2 (3), 297–308.

Busch, A., Bertier, P., Gensterblum, Y., Rother, G., Spiers, C.J., Zhang, M., Wentinck, H.J.M., 2016. On sorption and swelling of CO_2 in clays. Geomech. Geophys. Geo-Energy Geo-Resour. 1–20.

Colten-Bradley, V.A., 1987. Role of pressure in smectite dehydration—effects on geopressure and smectite-to-illite transformation. AAPG Bull. 71, 1414–1427.

De Jong, S.M., Spiers, C.J., Busch, A., 2014. Development of swelling strain in smectite clays through exposure to carbon dioxide. Int. J. Greenh. Gas Control 24, 149–161.

Eltantawy, I., Arnold, P., 1972. Adsorption of n-alkanes by Wyoming montmorillonite. Nature 237, 123–125.

Espinoza, D.N., Santamarina, J.C., 2012. Clay interaction with liquid and supercritical CO_2: The relevance of electrical and capillary forces. Int. J. Greenh. Gas Control 10, 351–362.

Espinoza, D.N., Vandamme, M., Pereira, J.M., Dangla, P., Vidal-Gilbert, S., 2014. Measurement and modeling of adsorptive–poromechanical properties of bituminous coal cores exposed to CO_2: adsorption, swelling strains, swelling stresses and impact on fracture permeability. Int. J. Coal Geol. 134, 80–95.

Espinoza, D.N., Pereira, J.M., Vandamme, M., Dangla, P., Vidal-Gilbert, S., 2015. Desorption-induced shear failure of coal bed seams during gas depletion. Int. J. Coal Geol. 137, 142–151.

Ferrage, E., Kirk, C.A., Cressey, G., Cuadros, J., 2007. Dehydration of Ca-montmorillonite at the crystal scale. Part I: Structure evolution. Am. Mineral. 92 (7), 994–1006.

Gaus, I., Azaroual, M., Czernichowski-Lauriol, I., 2005. Reactive transport modelling of the impact of CO2 injection on the clayey cap rock at Sleipner (North Sea). Chem. Geol. 217 (3-4), 319–337.

Gaus, I., 2010. Role and impact of CO_2–rock interactions during CO_2 storage in sedimentary rocks. Int. J. Greenh. Gas Control 4, 73–89.

Giesting, P., Guggenheim, S., Koster van Groos, A.F., Busch, A., 2012a. Interaction of carbon dioxide with Na-exchanged montmorillonite at pressures to 640bars: implications for CO_2 sequestration. Int. J. Greenh. Gas Control 8, 73–81.

Giesting, P., Guggenheim, S., Koster van Groos, A.F., Busch, A., 2012b. X-ray diffraction study of K- and Ca-exchanged montmorillonites in CO_2 atmospheres. Environ. Sci. Technol. 46 (10), 5623–5630.

Harward, M.E., Brindley, G.W., 1965. Swelling properties of synthetic smectites in relation to lattice substitutions. Clays Clay Miner. 13, 209–222.

Hatch, C.D., Wiese, J.S., Crane, C.C., Harris, K.J., Kloss, H.G., Baltrusaitis, J., 2012. Water adsorption on clay minerals as a function of relative humidity: application of BET and Freundlich adsorption models. Langmuir 28 (3), 1790–1803.

Hepple, R.P., Benson, S.M., 2005. Geologic storage of carbon dioxide as a climate change mitigation strategy: performance requirements and the implications of surface seepage. Environ. Geol. 47, 576–585.

Hol, S., Peach, C.J., Spiers, C.J., 2011. Applied stress reduces the CO_2 sorption capacity of coal. Int. J. Coal Geol. 85, 128–142.

Hol, S., Peach, C.J., Spiers, C.J., 2012. Effect of 3-D stress state on adsorption of CO_2 by coal. Int. J. Coal Geol. 93 (1), 1–15.

Hol, S., Gensterblum, Y., Massarotto, P., 2014. Sorption and changes in bulk modulus of coal—experimental evidence and governing mechanisms for CBM and ECBM applications. Int. J. Coal Geol. 128, 119–133.

Holloway, S., 1997. An overview of the underground disposal of carbon dioxide. Energy Convers. Manage. 38, S193–S198.

Horsrud, P., Sønstebø, E.F., Bøe, R., 1998. Mechanical and petrophysical properties of North Sea shales. Int. J. Rock Mech. Min. Sci. 35 (8), 1009–1020.

Hover, J., Eslinger, E.V., Hower, M.E., Perry, E.A., 1976. Mechanism of burial metamorphism of argillaceous sediment: 1. Mineralogical and chemical evidence. Geol. Soc. Am. Bull. 87, 725–737.

Hur, T.-B., Baltrus, J.P., Howard, B.H., Harbert, W.P., Romanov, V.N., 2013. Carbonate formation in Wyoming montmorillonite under high pressure carbon dioxide. Int. J. Greenhouse Gas Control 13, 149–155.

Ilton, E.S., Schaef, H.T., Qafoku, O., Rosso, K.M., Felmy, A.R., 2012. In situ X-ray diffraction study of Na+ saturated montmorillonite exposed to variably wet supercritical CO_2. Environ. Sci. Technol. 46 (7), 4241–4248.

Israelachvili, J.N., McGuiggan, P.M., Homola, A.M., 1988. Dynamic properties of molecularly thin liquidfilms. Science 240, 189–191.

Liteanu, E., Spiers, C.J., 2009. Influence of pore fluid salt content on compaction creep of calcite aggregates in the presence of supercritical CO_2. Chem. Geol. 265 (1–2), 134–147.

Liu, J., Peach, C.J., Zhou, H., Spiers, C.J., 2015. Thermodynamic models for swelling of unconfined coal due to adsorption of mixed gases. Fuel 157, 151–161.

Liu, J., Spiers, C.J., Peach, C.J., Vidal-Gilbert, S., 2016. Effect of lithostatic stress on methane sorption by coal: theory vs. experiment and implications for predicting in-situ coalbed methane content. Int. J. Coal Geol. 167, 48–64.

Loring, J.S., Schaef, H.T., Turcu, R.V.F., Thompson, C.J., Miller, Q.R.S., Martin, P.F., Hu, J.Z., Hoyt, D.W., Qafoku, O., Ilton, E.S., Felmy, A.R., Rosso, K.M., 2012. In situ molecular spectroscopic evidence for CO_2 intercalation into montmorillonite in supercritical carbon dioxide. Langmuir 28, 7125–7128.

Loring, J.S., Ilton, E.S., Chen, J., Thompson, C.J., Martin, P.F., Benezeth, P., Rosso, K.M., Felmy, A.R., Schaef, H.T., 2014. In situ study of CO_2 and H_2O partitioning between Na-montmorillonite and variably wet supercritical carbon dioxide. Langmuir 30, 6120–6128.

Lynch, F.L., 1997. Frio shale mineralogy and the stoichiometry of the smecitite-to-illite reaction: the most important reactioninclastic sedimentary diagenesis. Clays Clay Miner. 45, 618–631.

Michels, L., Fossum, J.O., Rozynek, Z., Hemmen, H., Rustenberg, K., Sobas, P.A., Kalantzopoulos, G.N., Knudsen, K.D., Janek, M., Plivelic, T.S., da Silva, G.J., 2015. Intercalation and retention of carbon dioxide in a smectite clay promoted by interlayer cations. Sci. Rep. 5, 8775.

Mooney, R.W., Keenan, A.G., Wood, L.A., 1952. Adsorption of water vapor by montmorillonite. II. Effect of exchangeable ions and lattice swelling as measured by X-ray diffraction. J. Am. Chem. Soc. 74 (6), 1371–1374.

Norrish, K., 1954. The swelling of montmorillonite. Discuss. Faraday Soc. 18, 120–134.

Orlic, B., ter Heege, J., Wassing, B.B.T., 2011. Assessing the short-term and long-term integrity of top seals in feasibility studies of geological CO_2 storage. 45th US Rock Mechanics/Geomechanics Symposium.

Ormerod, E.C., Newman, A.C.D., 1983. Water sorption on Ca-saturated clays: ||. Internal and external surfaces of montmorillonite. Clay Miner. 18, 289–299.

Pearson, M.J., 1990. Clay mineral distribution and provenance in Mesozoic and Tertiary mudrocks of the Moray Firth and northern North Sea. Clay Miner. 25, 519–541.

Prost, R., Koutit, T., Benchara, A., Huard, E., 1998. State and location of water adsorbed on clay minerals: consequences of the hydration and swelling-shrinkage phenomena. Clays Clay Miner. 46 (2), 117–131.

Renard, F., Ortoleva, P., 1997. Water films at grain–grain contacts: debye-Hückel, osmotic model of stress, salinity, and mineralogy dependence. Geochim. Cosmochim. Acta 61, 1963–1970.

Romanov, V.N., 2013. Evidence of irreversible CO_2 intercalation in montmorillonite. Int. J. Greenh. Gas Control 14, 220–226.

Rother, G., Ilton, E.S., Wallacher, D., Hauss, T., Schaef, H.T., Qafoku, O., Rosso, K.M., Felmy, A.R., Krukowski, E.G., Stack, A.G., Grimm, N., Bodnar, R.J., 2013. CO_2 sorption to subsingle hydration layer montmorillonite clay studied by excess sorption and neutron diffraction measurements. Environ. Sci. Technol. 47 (1), 205–211.

Rutter, E.H., 1983. Pressure solution in nature, theory, and experiment. J. Geol. Soc. Lond. 140, 725–740.

Sato, T., Watanabe, T., Otsuka, R., 1992. Effects of layer charge, charge location, and energy change on expansion properties of dioctahedral smectites. Clays Clay Miner. 40, 103–113.

Schaef, H.T., Ilton, E.S., Qafoku, O., Martin, P.F., Felmy, A.R., Rosso, K.M., 2012. In situ XRD study of Ca^{2+} saturated montmorillonite (STX-1) exposed to anhydrous and wet supercritical carbon dioxide. Int. J. Greenh. Gas Control 6, 220–229.

Schaef, H.T., Loring, J.S., Glezakou, V.A., Miller, Q.R.S., Chen, J., Owen, A.T., Lee, M.S., Ilton, E.S., Felmy, A.R., McGrail, B.P., Thompson, C.J., 2015. Competitive sorption of CO_2 and H_2O in 2:1 layer phyllosilicates. Geochim. Cosmochim. Acta 161, 248–257.

Shukla, R., Ranjith, P., Haque, A., Choi, X., 2010. A review of studies on CO_2 sequestration and caprock integrity. Fuel 89, 2651–2664.

Song, J., Zhang, D.X., 2013. Comprehensive review of caprock-sealing mechanisms for geologic carbon sequestration. Environ. Sci. Technol. 47, 9–22.

Sperner, B., Muller, B., Heidbach, O., Delvaux, D., Reinecker, J., Fuchs, K., 2003. Tectonic stress in the Earth's crust: advances in the World Stress Map project. Sp. Publ.-Geol. Soc. Lond. 212, 101–116.

Sposito, G., Prost, R., 1982. Structure of water adsorbed on smectites. Chem. Rev. 82 (6), 553–573.

UNFCCC, 2016. INDC Portal – INDCs as Communicated by Parties. Http://www4. unfccc.int/submissions/INDC/Submission%20Pages/submissions.aspx.

Van Olphen, H., Fripiat, J.J., 1979. Data Handbook for Clay Minerals and Other Non-Metallic Minerals. Pergamon Press, New York (346 pp.).

Wentinck, H.M., Busch, A., 2017. Modelling of CO_2 diffusion and related poro-elastic effects in a smectite-rich cap rock above a reservoir used for CO_2 storage. In: In: Rutter, E., Mecklenburgh, J., Taylor, K.G. (Eds.), Geomechanics and Petrophysical Properties of Mudrocks, vol. 454 Geological Society of London, London. http://dx.doi.org/10.1144/SP454.4. (Geological Society, London, Special Publications; Vol. 454).

Xu, W., Johnston, C.T., Parker, P., Agnew, S.F., 2000. Infrared studies of water sorption on Na-, Li-, Ca-, and Mg-exchanged (SWy-1 and SAz-1) montmorillonite. Clays Clay Miner. 48 (1), 120–131.

Zoback, M.L., 1992. First and second-order patterns of stress in the lithosphere: the World Stress Map Project. J. Geophys. Res. 97 (B8), 11703–11728.